Voltammetry of Porous Layers: Staircase vs Analog Voltammetry

Zhiyong Ban, Enno Kätelhön, Richard G Compton

Department of Chemistry, Physical and Theoretical Chemistry Laboratory, Oxford University, South Parks Road, Oxford, OX1 3QZ, United Kingdom

ABSTRACT

The use of staircase ramps for cyclic voltammetry rather than true linear analog ramps can lead to significant misinterpretation of the signals recorded for the measurement of diffusional redox species with either reversible or irreversible electrode kinetics measured at electrodes modified with porous layers. Most notably a large perturbation of the expected peak current is apparent which can preclude the extraction of meaningful data, for example in respect of surface coverages or in the identification of electro-catalysis.

Keywords: Porous electrodes, electrocatalysis, staircase voltammetry, voltammetry

INTRODUCTION

The voltammetric study of electrodes with porous surfaces is now commonplace since the use of nanoparticles and microparticles to attempt the electrocatalysis of diverse processes lies at the heart of energy transformation technology and much electroanalytical science. Electrochemical processes sought to be catalysed are as varied as the oxygen reduction reaction or the oxidation of glucose. Typical methodology involves the immobilisation of "designer" materials on the surface of an otherwise inert electrode, the measurement of cyclic voltammograms and the analysis of which seeks to identify useful changes in the electrochemical responses due to the presence of the modifying layer. This analysis is not trivial since any voltammetric response represents a subtle interplay between electron transfer kinetics, mass transport and the active surface area. Whilst this analysis is well established for flat, non-porous layers[1, 2] and developed to a high level of sophistication[3], such analysis represents at least a gross simplification for most porous surfaces and often is completely misleading. Thus we have shown that the transition from semi-infinite diffusion to thin layer diffusion has led to widespread misinterpretation of the voltammetry of carbon nanotube modified electrodes[4, 5] and explained the enhanced selectivity sometimes observed at such electrodes[6] in terms of changed mass transport regimes rather than electrocatalysis. The implications have been extended beyond cyclic and linear sweep voltammetry to differential pulse and square wave voltammetry[7]. Subsequent work showed a change of electrode geometry from flat and planar to non-flat and non-uniform (as for example in nanoparticle modified surfaces) could in itself lead to the false impression of a change of

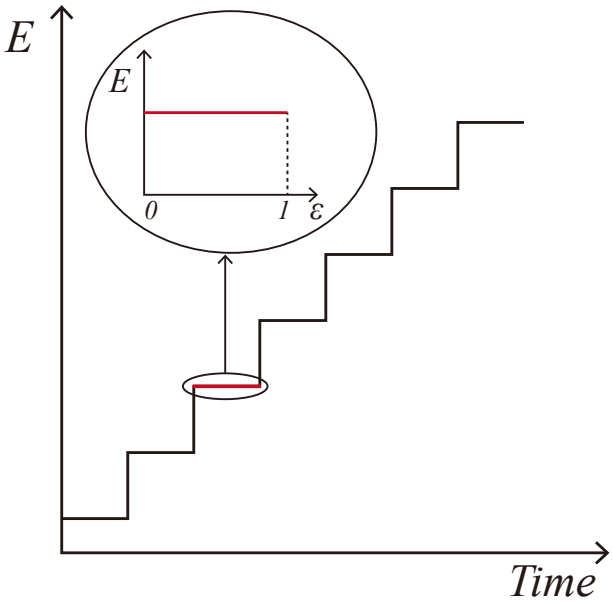

Figure 1: Plot of potential against time for staircase ramp voltammetry, E is potential and ϵ ($0 \leq \epsilon \leq 1$) is the point at which current is recorded on each step. [Figure was amended.]

electron transfer kinetics if data were to be analysised erroneously assuming the electrode to be of the former rather than the latter geometry[8, 9]. Similar conclusions were drawn in respect of rotating disc electrode voltammetry[10].

Most experimental voltammetry is today carried out using a staircase waveform (shown in Fig.1) to approximate the linear ramp typically underpinning the theory of cyclic and linear sweep voltammetry. The linear ramp is defined by the voltage scan rate whereas in the case of staircase voltammetry the step height, time step, and the point of current measurement ϵ ($0 \leq \epsilon \leq 1$) defines the applied potential form and resulting voltammetry (Fig.1). For flat, planar and uniform surfaces, it has been clearly established that discrepancies between staircase and true linear sweep voltammetry can easily arise[11–17]. Recommendations for the optimal selection of ϵ have been made[17–19] and correction factors have been reported[11]. Similar differences have been noted for microdisc voltammetry as well as for macroelectrodes[18].

In this paper we explore the implications of approximating true linear sweep voltammetry by staircase voltammetry for the study of diffusional processes at porous electrodes. Significant deviations are found with major implications for the possibility of important misinterpretation if the possibilities for differences are not recognised by experimentalists.

THEORETICAL MODEL

In this work, cyclic voltammetry at a porous electrode is simulated for the cases of true linear potential sweeps and staircase potential sweeps. The single-electron-transfer reaction,

$$A + e^- \rightleftharpoons B,$$

between two species with identical diffusion coefficients ($D_A = D_B = D$ (m^2 s^{-1})) is considered at the porous electrode surface.

The porous electrode is modelled as a series of uniformly distributed cylindrical protrusions of height z_e that expand from the electrode surface as shown in Fig.2a. All cylinders are considered to be identical so that the whole system can be represented in terms of a single cylinder within the diffusion domain approximation[20–24]. Thus the electrode surface is first divided into square unit cells each of equal area. Then, within the diffusion domain approximation we replace the square cells by circular cells with a surface area that is identical to the area of the square unit cell. Consequently, the cylinder coverage within the diffusion domain approximation is defined as: $r_e^2 \cdot r_{max}^{-2}$, where r_e and r_{max} are the radius of the cylinder and the diffusion domain circle, respectively. For a single cylinder, we hence simplify the model to a two-dimensional space as shown in Fig.2b, which is symmetrical with respect to the vertical z axis.

In our model, we assume that there is sufficient supporting electrolyte in the solution, which screens the electric field generated by the electrode[25]. As a result, mass transport exclusively occurs via diffusion without migration, which in the case of the given geometry follows Fick's Second Law[26]:

$$\frac{\partial c}{\partial t} = D\Big(\frac{\partial^2 c}{\partial r^2} + \frac{1}{r}\frac{\partial c}{\partial r} + \frac{\partial^2 c}{\partial z^2}\Big), \tag{1}$$

in cylindrical coordinates for an axially symmetrical system, where c $(mol\ m^{-3})$ is the concentration of either species A or B, D (m^2/s^{-1}) is the diffusion coefficient of either A or B, t (s) is the time, z (m) is the normal coordinate, and r (m) is the radial coordinate.

The electrode kinetics follow the Butler-Volmer model:

$$j = k_0 exp\Big(\frac{-\alpha F(E - E_f^0)}{\mathbb{R}T}\Big)c_A - k_0 exp\Big(\frac{+\beta F(E - E_f^0)}{\mathbb{R}T}\Big)c_B, \tag{2}$$

where j $(mol\ m^{-2}s^{-1})$ is the flux, c_A $(mol\ m^{-3})$ and c_B $(mol\ m^{-3})$ are the concentrations of A and B at the electrode surface respectively, α and β are transfer coefficients[27, 28], k_0 $(m\ s^{-1})$ is the electrochemical rate constant, E (V) is the electrode potential, E_f^0 (V) is the formal potential, $\mathbb{R}$ is the gas constant, and F and T have their usual significance.

The three-dimensional space shown in Fig.2b are transformed into the two-dimensional region shown in Fig.2c and the boundary conditions as follows.

1. At $z_{max} \geq z_e + 6\sqrt{D_A t_{max}}$ (where t_{max} is the duration of the simulation and z_e is the cylinder height), c_A and c_B are equal to their bulk values.

2. At $r = r_{max}$, $r = 0$ and the electrode base, the flux is equal to zero.

3. The top and side of the cylinder can be independently set to be either zero flux boundaries or electrodes with Butler-Volmer kinetics.

Both linear sweep and staircase potential cyclic voltammetry are simulated. For linear sweep cyclic voltammetry simulations, the potential E (V) follows the below relationship with time:

$$E(t) = \begin{cases} E_{max} - vt\ for\ \left(t < \dfrac{t_{max}}{2}\right) \\ E_{min} + v\left(t - \dfrac{t_{max}}{2}\right)\ for\ \left(t \geq \dfrac{t_{max}}{2}\right) \end{cases}, \tag{3}$$

where v $(V\ s^{-1})$ is the scan rate. The potential sweeps from E_{max} at $t = 0$ to E_{min} at $t = \frac{t_{max}}{2}$

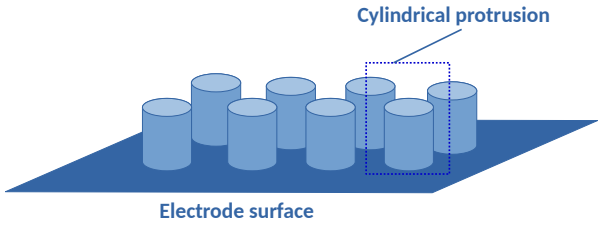

(a) Porous electrode model

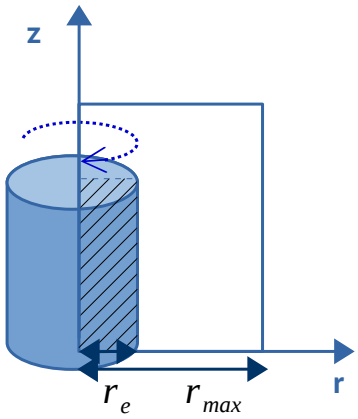

(b) A single cylinder in the diffusion domain approximation

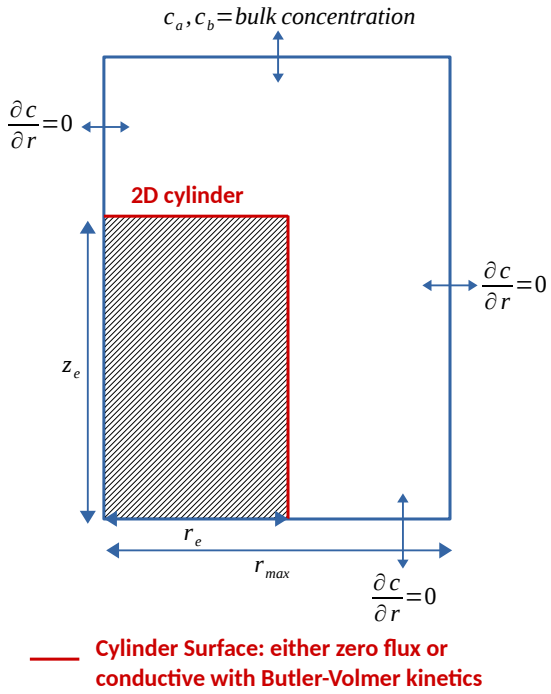

(c) 2D cross section of single cylinder

Figure 2: Porous electrode and simulation model

then back to E_{max} at $t = t_{max}$. For staircase potential voltammetry, when $t < \frac{t_{max}}{2}$, the potential decreases from E_{max} to E_{min} by "steps" featuring a "step height" of ΔE and increases in the same way when $t \geq \frac{t_{max}}{2}$ as follows:

$$E(t) = \begin{cases} E_{max} - \Delta E \sum_{n=1}^{n_{max}/2} H(t - n\Delta t) \ for \left(t < \frac{t_{max}}{2}\right) \\ E_{min} + \Delta E \sum_{n=1}^{n_{max}/2} H(t - \frac{t_{max}}{2} - n\Delta t) \ for \left(t \geq \frac{t_{max}}{2}\right) \end{cases}, \tag{4}$$

where H is the Heaviside step function, Δt is the time duration for each potential step, n is the step number and n_{max} is the maximum number of steps in the whole process.

COMPUTATIONAL STRATEGY AND METHODS

In this work, we employ dimensionless parameters to facilitate the scalability of our results unless units are specified. The dimensionless parameters can be calculated from their dimensional equivalents via the conventions[29] shown in Table.1

parameter	conversion
concentration	$C_j = \frac{c_j}{c_A^*}$
diffusion coefficient	$d_j = \frac{D_j}{D_A}$
radial distance	$R = \frac{r}{r_e}$
axial distance	$Z = \frac{z}{r_e}$
time	$\tau = \frac{D_A t}{r_e^2}$
rate constant	$K_0 = \frac{r_e k_0}{D_A}$
scan rate	$\sigma = \frac{r_e^2 F v}{D_A \mathbb{R} T}$
potential	$\theta = \frac{F(E-E_f^0)}{\mathbb{R}T}$
current	$J = \frac{I}{2\pi F r_e D_A c_A^*}$

Table 1: Conversion from dimensional parameters to dimensionless parameters. c_A^* $(mol\ m^{-3})$ is the bulk concentration of A, r_e (m) is the cylinder radius, I (A) is the current and all other symbols are defined in the text.

In the simulations, the two-dimensional space is discretised as an array of expanding grid[30, 31] points in R and Z direction. In the R direction, the spatial grid expands outwards from $R = 0$ and $R = R_e$, as follows[29]:

$$\begin{cases} R_i = R_{i-1} + h_0 \omega^{i-1} & for\ 0 < R \leq \dfrac{R_e}{2} \\ R_i = R_{i-1} + h_0 \omega^{n_e - i} & for\ \dfrac{R_e}{2} < R < R_e \\ R_i = R_{i-1} + h_0 \omega^{i-n_e-1} & for\ 1 \leq R \leq R_{max} \end{cases} \tag{5}$$

where R_i represents the i^{th} grid point in R direction, n_e is the number of grid points within $0 < R \leq R_e$, h_0 is the dimensionless distance between the first two grid points, and ω is the dimensionless expansion factor. The Z direction grid points are defined in the same way. We also discretise the time into time steps while adjacent time steps are separated by $\Delta\tau$.

Using the above-specified transformations, we obtain Fick's Second Law in dimensionless cylindrical coordinates:

$$\frac{\partial C}{\partial \tau} = \frac{\partial^2 C}{\partial R^2} + \frac{1}{R}\frac{\partial C}{\partial R} + \frac{\partial^2 C}{\partial Z^2}\ . \tag{6}$$

Within the finite difference model, this can be approximated as[29]:

$$\begin{aligned}\frac{C_{i,j}^{k}-C_{i,j}^{k-1}}{\Delta\tau} &= \left(\frac{C_{i+1,j}^{k}-C_{i,j}^{k}}{\Delta R_{+}}-\frac{C_{i,j}^{k}-C_{i-1,j}^{k}}{\Delta R_{-}}\right)\frac{2}{\Delta R_{-}+\Delta R_{+}} \\ &+\left(\frac{C_{i,j+1}^{k}-C_{i,j}^{k}}{\Delta Z_{+}}-\frac{C_{i,j}^{k}-C_{i,j-1}^{k}}{\Delta Z_{-}}\right)\frac{2}{\Delta Z_{+}+\Delta Z_{-}} \\ &+\frac{1}{R_i}\left(\frac{C_{i+1,j}^{k}-C_{i-1,j}^{k}}{\Delta R_{+}+\Delta R_{-}}\right),\end{aligned} \tag{7}$$

where $C_{i,j}^{k}$ is the concentration of species (either A or B) at the k^{th} time step at the position of the i^{th} grid point in R direction and the j^{th} in Z direction, ΔR_{+} is the spatial separation between the $(i+1)^{th}$ and the i^{th} grid point in R direction, ΔR_{-} is the spatial separation between the i^{th} and the $(i-1)^{th}$ grid point in R direction and ΔZ_{+} and ΔZ_{-} are defined in the same manner.

We use the alternating direction implicit (ADI) method[32–34] to solve eqn.(7), in which each time step is divided in two half time steps. In the first half time step, an implicit method is used to solve eqn.(7) along the Z direction and an explicit method is used along the R direction, and vice versa for the second half time step. The Thomas Algorithm[35] is used to solve the tridiagonal matrix obtained from each half time step.

The dimensionless current J is calculated from:

$$J=\int_{0}^{R_e}-\Big(\frac{\partial C}{\partial Z}\Big)_{Z=Z_e}RdR \tag{8}$$

after the first half time step or from:

$$J=\int_{0}^{Z_e}-\Big(\frac{\partial C}{\partial R}\Big)_{R=R_e}dZ \tag{9}$$

after second half time step at the respective surface. We measure the current for each electrode surface (top or side) separately, in the case of both the top and side surfaces being conductive, the sum of two currents is calculated.

In this work, all simulations are written in C++ and simulations were subjected to convergence tests[36]. The results for "reversible kinetics" and "irreversible kinetics" are simulated using moderate h_0, ω and time step values so that the average runtime is about 10 minutes on a desktop computer with 16-core CPU. In the convergence tests, we decrease these parameter values for a higher accuracy of the result, leading to the average runtime increases to approximately four hours. The peak currents of the results used in this paper are compared to the convergence test results and the percentage difference is always found to be less than 2%. In the staircase potential simulations, the average runtime is chosen to be about 8 hours in order to achieve a more accurate result, as discussed below.

In all simulations, $\alpha=\beta=0.5$, a bulk concentration $c_A^*=1000(mol\ m^{-3})$ $(C_A^*=1)$, $c_B^*=0(mol\ m^{-3})$ $(C_b^*=0)$, diffusion coefficients $D_A=D_B=1.183\times10^{-9}$ $(m^2\ s^{-1})$ $(d_a=d_b=1)$, which is the value for potassium ferrocyanide anions[37], the cylinder radius $r_e=10^{-7}(m)$ $(R_e=1)$ and for the staircase potential voltammetry, the stair height $\Delta E=2.05$ (mV) $(\Delta\theta=0.08)$.

R_{max}, Z_e, the scan rate σ and the rate constant K_0 are varied to achieve different simulated results.

RESULTS AND DISCUSSION

In the following sections, we separately discuss the results of simulations for reversible and irreversible electrode kinetics using a true linear voltage ramp and then compare these with the results for staircase ramps. In order to explain the full simulation results we make recourse to two familiar different limiting cases as follows.

(a) The thin layer model. In this case the solution between the walls of the electrode and the boundary of the diffusion domain is assumed to be nearly exhaustively electrolysed on the timescale of the voltammetric sweep. Thus the annular gap between the two surfaces acts as a "thin layer" cell [38, 39] for which the following equation holds for Nernstian voltammetry:

$$I_p = \frac{F^2}{4\mathbb{R}T} v V c_{tot}, \tag{10}$$

where I_p is the peak current, v is the scan rate, V is the volume of the annular gap and other symbols are as defined previously. The peak to peak separation, ΔE_{pp}, is zero[39–41].

(b) The Randles-Ševčík model. Diffusion to the top of the electrode and to the walls of the electrode can be viewed under fast scan rate conditions as being semi-infinite for which the current to an electrode of surface area A is given by:

$$I_p = 0.446 F A c_A^* \sqrt{\frac{F D v}{\mathbb{R}T}}, \tag{11}$$

and the peak to peak separation is given by:

$$\begin{aligned} \Delta E_{pp} &= 2.218 \frac{\mathbb{R}T}{F} \\ &= 57 \ (mV) \ at \ 298K, \end{aligned} \tag{12}$$

for reversible electrode kinetics. In the following, the above two equations are applied to either the top or the side of the electrode. In addition under some circumstances (see below) the diffusion to the entire electrode reflects the area of the diffusion domain (πr_{max}^2) rather than that of the electrode (πr_e^2).

Reversible kinetics

In the case of reversible electrode kinetics, taking an artificially high value of $K_0 = 10^6$ to ensure "Nernstian" behaviour, we simulated the linear ramp cyclic voltammetry for different cylinder geometries. To obtain cyclic voltammetry behaviour, the dimensionless potential θ scans from 20 to -20 then back to 20.

The simulation results of the "both top and side active" cylinder are shown in Fig.3. The dots and crosses are the simulated $log(J_p)$ and $\Delta\theta_{pp}$ against $log(\sigma)$ respectively, where J_p is the dimensionless peak current and $\Delta\theta_{pp}$ is the dimensionless peak to peak separation. It can be

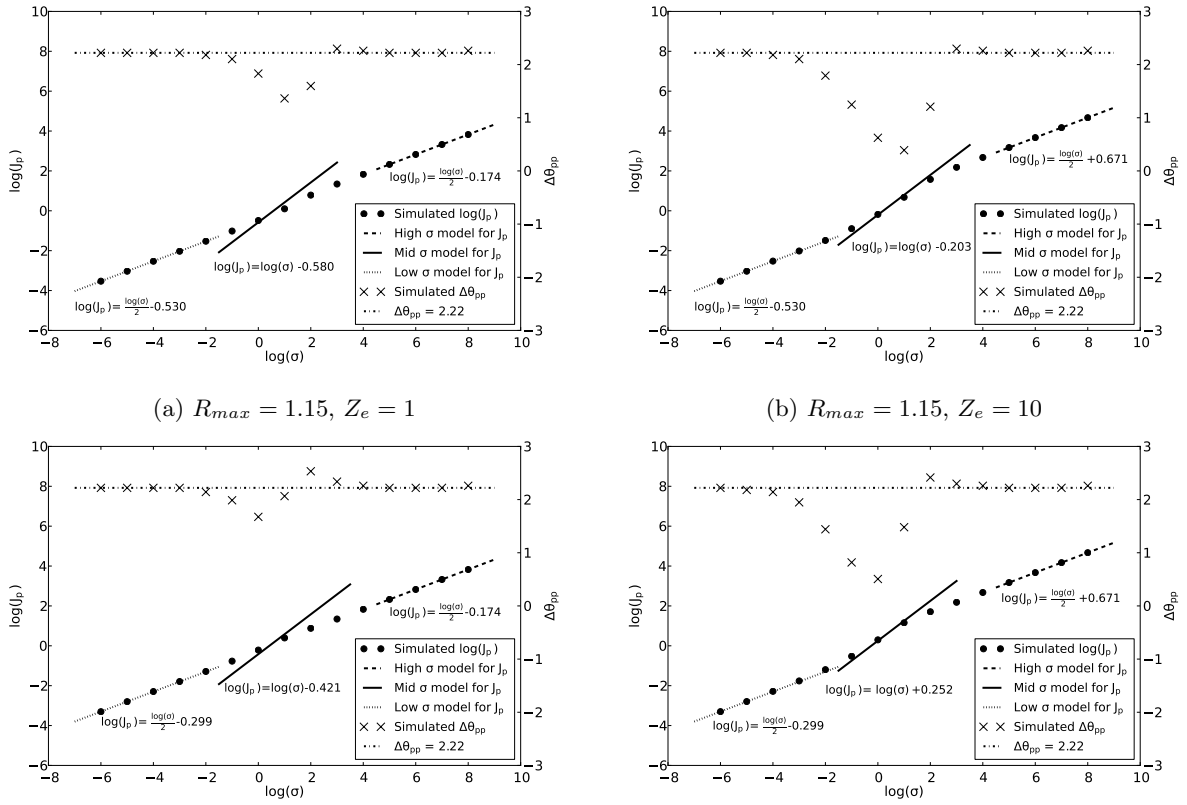

(a) $R_{max} = 1.15$, $Z_e = 1$

(b) $R_{max} = 1.15$, $Z_e = 10$

(c) $R_{max} = 1.5$, $Z_e = 1$

(d) $R_{max} = 1.5$, $Z_e = 10$

Figure 3: Plot of the dimensionless $log(J_p)$ and $\Delta\theta_{pp}$ against $log(\sigma)$ with reversible kinetics, $K_0 = 10^6$ for different geometries. Both top and side of the cylinder are active.

seen from figures that the peak currents can be divided into three segments at large, intermediate and small scan rate (σ) regions.

The simulated peak currents in the large and small scan rate limits perfectly match with the Randles-Ševčík model (shown in Fig.3) for all of the cylinder geometries, which is discussed below. The black line in Fig.3 shows the peak currents for thin layer diffusion model applied to the medium scan rate range. Note, as expected, the thin layer diffusion approximation exhibits better agreement in the case of the long cylinder (i.e. $Z_e = 10$).

For large scan rates, the diffusion occurs close to the electrode surface and can be approximated as one-dimensional. The peak currents for the "both top and side active" cylinders match with the dimensionless reversible Randles-Ševčík equation for semi-infinite diffusion:

$$J_p = 0.446 Z_e \sqrt{\sigma} + \frac{0.446}{2}\sqrt{\sigma}, \tag{13}$$

where the first and second term correspond to the current at the side and the top of the cylinder, respectively. In the case of only one surface of cylinder being conductive, we modify the eqn.(13) in a way that we solely evaluate the respective term, for example, $J_p = 0.446 Z_e \sqrt{\sigma}$ for "side active" cylinders.

In the small σ limit, the sweep is slow compared to the time required to establish a local concentration equilibrium within the region surrounding the cylinder at the bottom of the simulated cylindrical space. This allows the establishing of a near equilibrium within the pore and

above the cylinder and a significant gradient in the diffusing substance's concentration can only be found far from the electrode surface. As a result of this, only planar diffusion can be found towards the bottom of the simulated cylindrical space, which can be approximated as a macrodisk electrode with the radius $R = R_{max}$. The peak currents follow the reversible Randles-Ševčík equation for planar diffusion:

$$J_p = \frac{0.446}{2} R_{max}^2 \sqrt{\sigma}, \tag{14}$$

which is universally applicable for all of three cases for "both top and side active", "side active only" and "top active only" cylinders.

For medium scan rates, the peak currents for thin layer diffusion model on the side of the cylinder can then be expressed as[2]:

$$J_p = \frac{1}{8}(C_A^* + C_B^*)(R_{max}^2 - R_e^2) Z_e \sigma. \tag{15}$$

It is clear from the figures that the thin layer diffusion model cannot be applied to the case of short cylinder geometries. We attribute this to the fact that there is insufficient A in the small pore to enable dominant thin layer behaviour so that the effect of planar diffusion is predominant, and that there is significant diffusion out of the pore. However, as the height of the cylinder increases, the thin layer behaviour becomes more evident.

We additionally compared the simulated peak to peak separations to the reversible Randles-Ševčík limiting value ($\Delta\theta_{pp} = 2.22$ [40, 41]), shown in Fig.3. In the large and small scan rate limits, the simulated $\Delta\theta_{pp}$ values reflect the theoretical value. At the medium scan rate range, deviations for $\Delta\theta_{pp}$ are observed. Fig.3 also reveals the dip in $\Delta\theta_{pp}$ for $Z_e = 10$ (long cylinder) at the middle is much larger than that found for smaller Z_e values.

In thin layer diffusion model, within the pore, the diffusion gradient is zero and the concentration at any position is essentially uniform, hence leading to a zero peak to peak separation and the voltammetry to be symmetrical with respect to the formal potential. The fact that the long cylinder geometries agree better with the thin layer diffusion model (larger dip) indicates that most of the signal is dominated by thin layer effects as expected. However, at $log(\sigma)$ equal to about 2, $\Delta\theta_{pp}$ exceeds 2.22; this is discussed below.

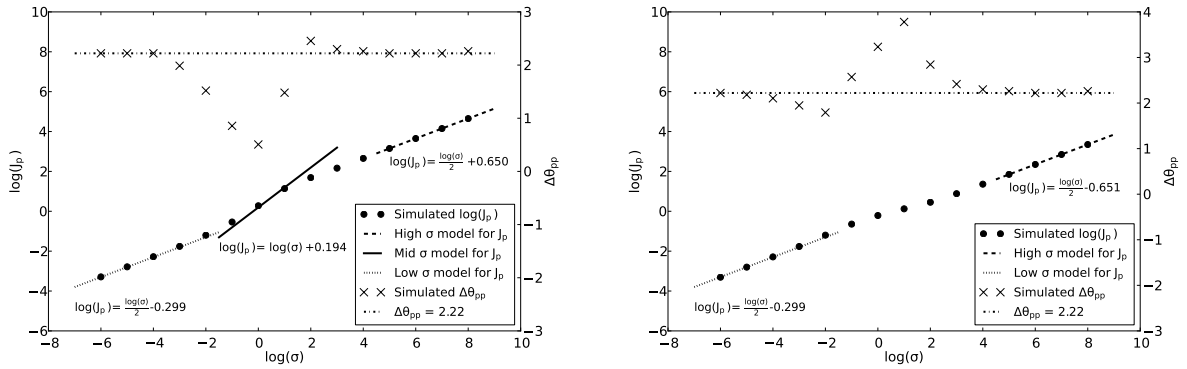

(a) "side active only" cylinder

(b) "top active only" cylinder

Figure 4: Plot of the dimensionless $log(J_p)$ and $\Delta\theta_{pp}$ against $log(\sigma)$ with reversible kinetics, $K_0 = 10^6$, $R_{max} = 1.5$ and $Z_e = 10$ for "side active only" and "top active only" cylinder.

Fig.4 shows the same plots as Fig.3, for "side active only" and "top active only" cylinders. In the "side active only" cylinder case (shown as Fig.4a), the result is similar to that of the "both top and side" active case, which means the peak currents follow the Randles-Ševčík model and the thin layer model as well and the peak to peak separation dips at the middle. For the "top active only" cylinder (shown as Fig.4b), the simulated peak currents in the two limits still match with the Randles-Ševčík model, however, as the side of the cylinder is not conductive, there is no thin layer model to predict the the medium scan rate region. In this case the dimensionless peak to peak separation is much greater than 2.22.

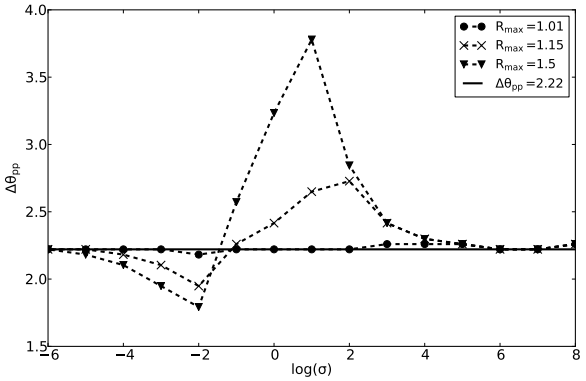

Figure 5: Plot of the dimensionless $\Delta\theta_{pp}$ against $log(\sigma)$ with "top active only" cylinder, $Z_e = 10$ and $K_0 = 10^6$ for $R_{max} = 1.01,\ 1.15,\ 1.5$ respectively.

The plot of the $\Delta\theta_{pp}$ against $log(\sigma)$ for three different R_{max} values is shown in Fig.5 for this "top active" case. Perhaps counter-intuitively, $\Delta\theta_{pp}$ increases at the medium σ range, which is opposed to the thin layer behaviour. This effect increases as R_{max} becomes larger. This is because the diffusion from within the pore towards the top of the cylinder, which is the only active surface, accounts for this seemingly "irreversible" behaviour even though the reaction is reversible. This insight also explains why $\Delta\theta_{pp}$ exceeds 2.22 (at about $log(\sigma)$ equal to 2) in the "top and side active" simulations.

Irreversible kinetics

We simulated the linear ramp cyclic voltammetries with fully irreversible kinetics, $K_0 = 10^{-6}$, for "side active only" cylinders and "top and side active" cylinders. In this case, the dimensionless potential, θ, sweeps from 40 to -40 then back to 40.

Fig.6a shows the plot of $log(J_p)$ against $log(\sigma)$ for a "top and side active" cylinder with $R_{max} = 1.15$ and $Z_e = 10$. The dots are the simulated $log(J_p)$ values and both the Randles-

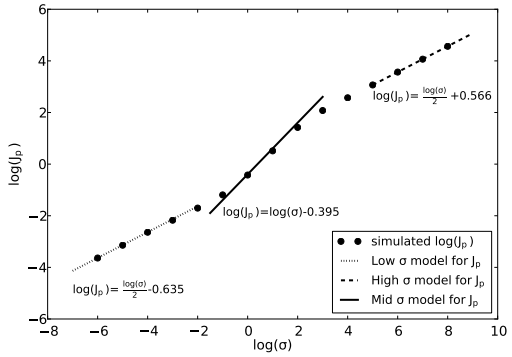

(a) Plot of the dimensionless $log(J_p)$ against $log(\sigma)$ with $R_{max} = 1.15$, $Z_e = 10$.

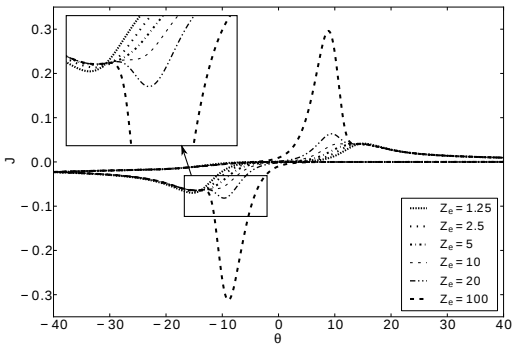

(b) Plot of the dimensionless cyclic voltammograms with $R_{max} = 1.15$, $\sigma = 0.1$ for different Z_e values.

Figure 6: Irreversible simulations of "both top and side active" cylinders, $K_0 = 10^{-6}$.

Ševčík model for irreversible electrode kinetics and the thin layer model are plotted. Similarly, it can be clearly seen that the Randles-Ševčík model and the thin layer model, as discussed above, can analogously be applied to irreversible kinetics.

For the "both top and side active" cylinders, the peak current J_p in the large σ limit is well predicted by the irreversible Randles-Ševčík model, given by:

$$J_p = 0.496 Z_e \sqrt{\alpha\sigma} + \frac{0.496}{2}\sqrt{\alpha\sigma}, \tag{16}$$

while in the small σ limit follows:

$$J_p = \frac{0.496}{2} R_{max}^2 \sqrt{\alpha\sigma}, \tag{17}$$

and in the medium σ region, the thin layer prediction remains unchanged as eqn.(15). In this case, Z_e is large and thin layer diffusion model can be applied to it as discussed previously. Modification for other cylinder types are made as mentioned in the reversible case.

Voltammograms with different Z_e values for "both top and side active" cylinders with $R_e = 10$ and $\sigma = 0.1$ are shown in Fig.6b. It is evident that, within $-1 < log(\sigma) < 2$, two forward peaks are found in the long cylinder geometry cases and the first peak (at about $\theta = -10$) rises, but the second peak(at about $\theta = -15$) decreases as the cylinder becomes longer.

It has been suggested the first peak is due to thin layer diffusion and the second peak is due to planar diffusion[42]. For the cylinders with small Z_e values, as mentioned in the above case, it is the insufficiency of the amount of the substance within the pore, the influence of planar diffusion, and diffusion from the inside to the outside of the pore leading to the thin layer peak being less pronounced. As Z_e increases, the significance of thin layer diffusion becomes enhanced while planar diffusion to the cylinder top remains unchanged except for a small amount of the substance in its diffusion field that interferes differently with the pore. Consequently, the first peak grows and the second peak decreases to a small extent with Z_e.

We simulated "side active" cylinder case as well and two forwards peaks can still be observed at the medium scan rate region. However, for "top active" cylinders, the peak splitting in the voltammogram is not found because when the side of the cylinder is not conductive, there is no thin layer diffusion within the annular gap.

Staircase potential sweeps

The above simulations model true voltammetry using a linear ramp, whereas, in reality, modern potentiostats apply potential steps rather than linear potential sweeps as discussed above. In this section, we study staircase ramp cyclic voltammetry at the "side active only" cylinder. We use dimensional parameters for the convenience of comparing the results to practical experimental results. In the simulations, a step height of $\Delta E = 2.05\ (mV)$ is used; the electrode potential E sweeps from $0.513\ (V)$ to $-0.513\ (V)$ then back to $0.513\ (V)$ for reversible reactions and from $1.03\ (V)$ to $-1.03\ (V)$ then returns $1.03\ (V)$ for irreversible reactions; the diffusion coefficients for A and B are both equal to $1.20\times10^{-9}(m^2s^{-1})$; $r_e = 10\ (\mu m)$, $z_e = 100\ (\mu m)$ and $r_{max} = 11\ (\mu m)$; the reversible kinetics are modelled with an artificially fast $k_0 = 1.2 \times 10^4\ (cm \cdot s^{-1})$ to ensure "Nernstian behaviour" and the irreversible simulations use $k_0 = 1.2 \times 10^{-5}\ (cm \cdot s^{-1})$.

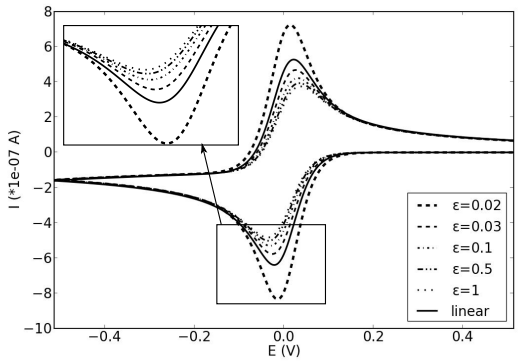

(a) scan rate (v) = 0.025 (Vs^{-1})

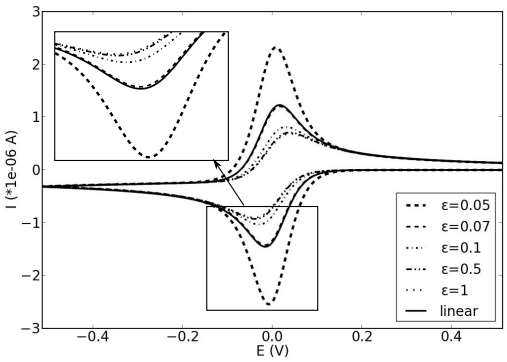

(b) scan rate (v) = 0.1 (Vs^{-1})

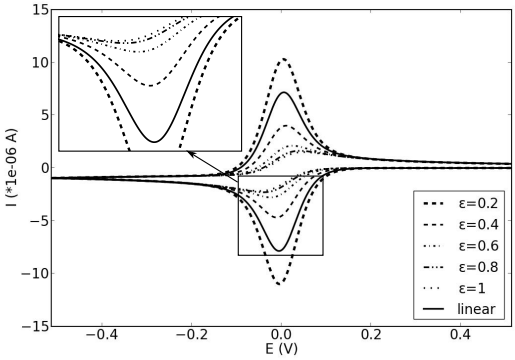

(c) scan rate (v) = 1.0 (Vs^{-1})

Figure 7: Plots of the voltammograms with "side active only" cylinder, $r_e = 10$ (μm), $z_e = 100$ (μm), $r_{max} = 11$ (μm), $D_A = D_B = 1.20 \times 10^{-9}$ ($m^2 s^{-1}$) and $k_0 = 12000$ ($cm \cdot s^{-1}$) (ensuring "reversible Nernstian behaviour"). The linear ramp simulation results using the same parameters are shown as solid lines and the other discontinuous lines are the staircase ramp results. [Figure was amended.]

In the staircase simulations, due to the approximations made in the ADI method, the result is convergent only if the total number of timestep is large. In order to achieve better results, we increase the number of time steps for each simulation and hence the average runtime for these simulations is about 21 hours on a 16-core CPU desktop computer.

Fig.7 displays three voltammograms simulated at different scan rates for reversible kinetics. For the staircase ramp simulations, voltammograms were recorded at various ϵ values. We define ϵ as the point, at which the current is recorded during each potential step, and it equals 0 immediately after the potential rises to a new step and 1 at the last moment of the same step (see Fig.1).

As it can be seen from the plots, changes in the voltammograms are found in the staircase simulations (shown as discontinuous lines) as a function of ϵ and the variation strong at small ϵ values. Furthermore, comparing to true linear ramp simulations (shown as solid lines), deviations can be significant depending on ϵ. For the cases of $v = 0.025$ (Vs^{-1}) (Fig.7a) and $v = 0.1$ (Vs^{-1}) (Fig.7b), the true linear ramp simulation voltammograms lie within the region ϵ smaller than 0.1. For $v = 1.0$ (Vs^{-1}) (Fig.7c), the true linear ramp result is found at ϵ between 0.2 and 0.4.

In the case of $v = 1.0(Vs^{-1})$, at ϵ equals 0.2 and 0.4, the voltammograms exhibit dominant symmetrical components with respect to the applied potential and the peak to peak separations are approximately zero. The linear sweep simulation gives a similar voltammogram, which

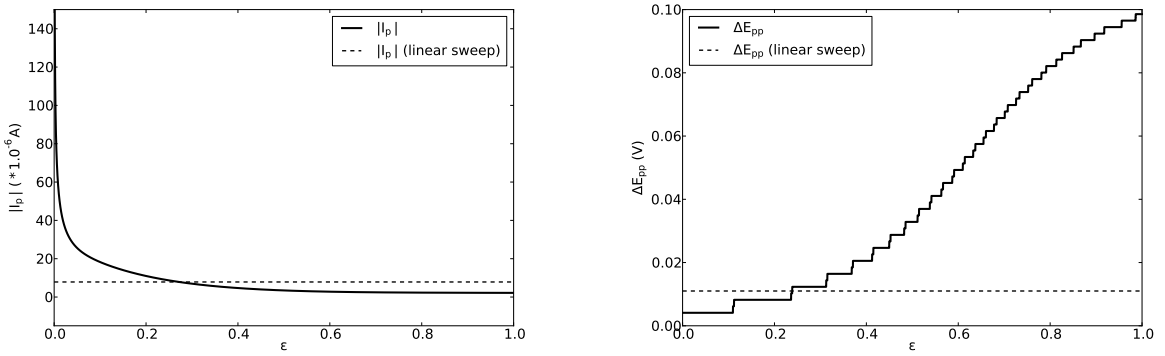

(a) $|I_p|$ against ϵ

(b) ΔE_{pp} against ϵ

Figure 8: Plots of absolute peak currents and peak to peak separations against ϵ for "side active only" cylinder, scan rate $(v) = 1\ (Vs^{-1})$, $r_e = 10\ (\mu m)$, $z_e = 100\ (\mu m)$, $r_{max} = 11\ (\mu m)$, $D_A = D_B = 1.20 \times 10^{-9}\ (m^2 s^{-1})$ and $k_0 = 12000\ (cm \cdot s^{-1})$ (ensuring "reversible Nernstian behaviour"). The dotted lines are the linear ramp simulation results and the solid lines are the results from staircase simulations. [Figure was amended.]

suggests that thin layer behaviour can be found within the pore for the reason as mentioned above.

In order to study the relation between the voltammogram and ϵ in detail, we additionally plotted the absolute peak currents and peak to peak separations as a function of ϵ (shown in Fig.8) for the case of $v = 1.0\ (Vs^{-1})$. The solid lines and dotted lines represent the results from staircase and true linear sweep simulations, respectively. Both plots in Fig.8 are consistent with the fact that the true linear ramp result is located between ϵ equals 0.2 and 0.4 in this case.

It is evident from Fig.8a that the peak current decays to approximately zero, leading to significant underestimated of the current at high ϵ values. The reason for this behaviour is that, on small time scales, the voltammetries can be considered as potential step chronoamperometry as the voltage increases to a new step abruptly and stays at the same value for a period.

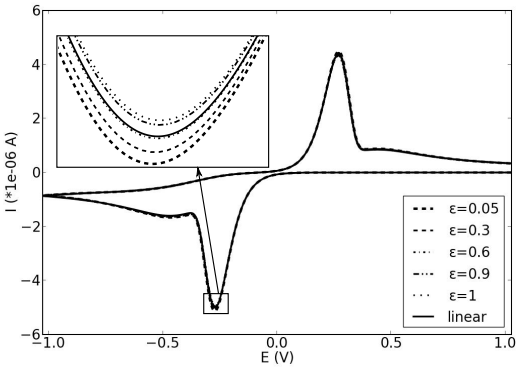

Figure 9: Plot of voltammograms with irreversible kinetics, $k_0 = 1.2 \times 10^{-5}\ (cm \cdot s^{-1})$. Other parameters are the same as Fig.8 simulation.

The peak to peak separation plotted in Fig.8b shows an increasing trend in peak to peak separation with ϵ and the slope is the steepest at the middle ϵ region. It is worth noticing that the peak to peak separation exceeds 57 (mV), which is the limiting value for reversible kinetics at 298K in the case of linear sweep voltammetry at macro- and microdisk electrodes, when ϵ is larger than 0.6. However, in real experiments, currents are often recorded at ϵ equal to 1 and, accordingly, it may wrongly imply irreversible behaviour $(\Delta E_{pp} > 57\ (mV))$ even though reversible kinetics are present. Moreover, as Fig.8a shows large ϵ significantly undermeasures the current.

We simulated irreversible kinetics reaction using $k_0 = 1.2 \times 10^{-5}\ (cm \cdot s^{-1})$(shown in Fig.9) while other parameters remain the same as the simulation shown in Fig.8. The voltammograms in Fig.9 reveal the variation in voltammetry against ϵ whilst not as obvious as that under

reversible kinetics and two forward peaks are found, that are still significant. An enlarged region for the first peak (thin layer peak) is shown in the plot, and the true linear sweep voltammogram is found to be above the one recorded at ϵ= 0.6.

Last, it should be noted that capacitive charging of double layers may additionally obscure the shape of recorded voltammograms. These can be very considerable in the case of porous layers and this provides a further reason for the need for careful analysis of experimental data.

CONCLUSIONS

In conclusion, for staircase voltammetry especially for reversible kinetics, the voltammogram significantly depends on ϵ. The absolute peak current decreases with ϵ, and the peak to peak separation increases with ϵ. The correspondence with the true linear sweep voltammogram lies at different ϵ values when different scan rates are used. In particular, experimentalists need to exercise due caution in using staircase voltammetry for the study of electrodes modified with porous layers not least since the default option in many potentiostats sets ϵ equal to 1.0 where errors are significant.

ACKNOWLEDGEMENT

The research leading to these results has received partial funding from the European Research Council under the European Union's Seventh Framework Programme (FP/2007-2013) / ERC Grand Agreement n. [320403].

References

[1] Allen J Bard and Larry R Faulkner. *Electrochemical methods: fundamentals and applications 2nd Edition*. Wiley New York, 2000.

[2] Richard G Compton and Craig E Banks. *Understanding voltammetry 2nd Edition*. World Scientific, 2011.

[3] Christopher Batchelor-McAuley, Enno Kätelhön, Edward O Barnes, Richard G Compton, Eduardo Laborda, and Angela Molina. Recent advances in voltammetry. *Chemistry Open*, 4(3):224–260, 2015.

[4] Ian Streeter, Gregory G Wildgoose, Lidong Shao, and Richard G Compton. Cyclic voltammetry on electrode surfaces covered with porous layers: An analysis of electron transfer kinetics at single-walled carbon nanotube modified electrodes. *Sensors and Actuators B: Chemical*, 133(2):462–466, 2008.

[5] Marcus J Sims, Neil V Rees, Edmund JF Dickinson, and Richard G Compton. Effects of thin-layer diffusion in the electrochemical detection of nicotine on basal plane pyrolytic graphite electrodes modified with layers of multi-walled carbon nanotubes. *Sensors and Actuators B: Chemical*, 144(1):153–158, 2010.

[6] Martin C Henstridge, Edmund JF Dickinson, Mehmet Aslanoglu, Christopher Batchelor-McAuley, and Richard G Compton. Voltammetric selectivity conferred by the modification of electrodes using conductive porous layers or films: The oxidation of dopamine on glassy carbon electrodes modified with multiwalled carbon nanotubes. *Sensors and Actuators B: Chemical*, 145(1):417–427, 2010.

[7] Eduardo Laborda, Angela Molina, Francisco Martínez-Ortiz, and Richard G Compton. Electrode modification using porous layers. Maximising the analytical response by choosing the most suitable voltammetry: Differential pulse vs square wave vs linear sweep voltammetry. *Electrochimica Acta*, 73:3–9, 2012.

[8] Kristopher R Ward, Matthew Gara, Nathan S Lawrence, R Seth Hartshorne, and Richard G Compton. Nanoparticle modified electrodes can show an apparent increase in electrode kinetics due solely to altered surface geometry: The effective electrochemical rate constant for non-flat and non-uniform electrode surfaces. *Journal of Electroanalytical Chemistry*, 695:1–9, 2013.

[9] Kristopher R Ward and Richard G Compton. Quantifying the apparent catalytic effect of porous electrode surfaces. *Journal of Electroanalytical Chemistry*, 724:43–47, 2014.

[10] Justus Masa, Christopher Batchelor-McAuley, Wolfgang Schuhmann, and Richard G Compton. Koutecky-levich analysis applied to nanoparticle modified rotating disk electrodes: electrocatalysis or misinterpretation. *Nano Research*, 7(1):71–78, 2014.

[11] Christopher Batchelor-McAuley, Minjun Yang, Elise M Hall, and Richard G Compton. Correction factors for the analysis of voltammetric peak currents measured using staircase voltammetry. *Journal of Electroanalytical Chemistry*, 758:1–6, 2015.

[12] Renata Bilewicz, Robert A Osteryoung, and Janet Osteryoung. Comparison of linear scan and staircase voltammetry: experimental results. *Analytical Chemistry*, 58(13):2761–2765, 1986.

[13] Renata Bilewicz, Kazimierz Wikiel, Robert A Osteryoung, and Janet Osteryoung. General equivalence of linear scan and staircase voltammetry: experimental results. *Analytical Chemistry*, 61(9):965–972, 1989.

[14] Mary M Murphy, John J O'Dea, Dieter Arn, and Janet Osteryoung. Theory of cyclic staircase voltammetry for electrode kinetics. *Analytical Chemistry*, 61(20):2249–2254, 1989.

[15] Mary M Murphy, John J O'Dea, Dieter Arn, and Janet Osteryoung. Theory for cyclic staircase voltammetry for first-order coupled reactions. *Analytical Chemistry*, 62(9):903–909, 1990.

[16] M Seralathan, Robert A Osteryoung, and Janet Osteryoung. Comparison of linear sweep and staircase voltammetries using walsh series. *Journal of electroanalytical chemistry and interfacial electrochemistry*, 214(1-2):141–156, 1986.

[17] M Seralathan, Robert A Osteryoung, and Janet Osteryoung. General equivalence of linear scan and staircase voltammetry. *Journal of electroanalytical chemistry and interfacial electrochemistry*, 222(1):69–100, 1987.

[18] Alexander S Barnes, Ian Streeter, and Richard G Compton. On the use of digital staircase ramps for linear sweep voltammetry at microdisc electrodes: Large step potentials significantly broaden and shift voltammetric peaks. *Journal of Electroanalytical Chemistry*, 623 (1):129–133, 2008.

[19] Uruthirapasupathy Kalapathy and Dennis E Tallman. Equivalence of staircase and linear sweep voltammetries for reversible systems including conditions of convergent diffusion. *Analytical Chemistry*, 64(22):2693–2700, 1992.

[20] Trevor J Davies, Craig E Banks, and Richard G Compton. Voltammetry at spatially heterogeneous electrodes. *Journal of solid state electrochemistry*, 9(12):797–808, 2005.

[21] Benjamin R Scharifker. Diffusion to ensembles of microelectrodes. *Journal of electroanalytical chemistry and interfacial electrochemistry*, 240(1-2):61–76, 1988.

[22] Oleksii Sliusarenko, Alexander Oleinick, Irina Svir, and Christian Amatore. Validating a central approximation in theories of regular electrode electrochemical arrays of various common geometries. *Electroanalysis*, 27(4):980–991, 2015.

[23] Neus Godino, Xavier Borrise, Francesc Xavier Munoz, Francisco Javier Del Campo, and Richard G Compton. Mass transport to nanoelectrode arrays and limitations of the diffusion domain approach: theory and experiment. *The Journal of Physical Chemistry C*, 113(25): 11119–11125, 2009.

[24] Benjamin A Brookes, Trevor J Davies, Adrian C Fisher, Russell G Evans, Shelley J Wilkins, Kamran Yunus, Jay D Wadhawan, and Richard G Compton. Computational and experimental study of the cyclic voltammetry response of partially blocked electrodes. part 1. nonoverlapping, uniformly distributed blocking systems. *The Journal of Physical Chemistry B*, 107(7):1616–1627, 2003.

[25] Edmund JF Dickinson, Juan G Limon-Petersen, Neil V Rees, and Richard G Compton. How much supporting electrolyte is required to make a cyclic voltammetry experiment quantitatively diffusional? A theoretical and experimental investigation. *The Journal of Physical Chemistry C*, 113(25):11157–11171, 2009.

[26] Adolph Fick. On liquid diffusion. *Journal of Membrane Science*, 100(1):33–38, 1995.

[27] Rolando Guidelli, Richard G Compton, Juan M Feliu, Eliezer Gileadi, Jacek Lipkowski, Wolfgang Schmickler, and Sergio Trasatti. Defining the transfer coefficient in electrochemistry: An assessment (IUPAC technical report). *Pure and Applied Chemistry*, 86(2):245–258, 2014.

[28] Rolando Guidelli, Richard G Compton, Juan M Feliu, Eliezer Gileadi, Jacek Lipkowski, Wolfgang Schmickler, and Sergio Trasatti. Definition of the transfer coefficient in electrochemistry (IUPAC recommendations 2014). *Pure and Applied Chemistry*, 86(2):259–262, 2014.

[29] Richard G Compton, Eduardo Laborda, and Kristopher R Ward. *Understanding voltammetry: simulation of electrode processes*. Imperial College Press, 2013.

[30] Stephen W Feldberg. Optimization of explicit finite-difference simulation of electrochemical phenomena utilizing an exponentially expanded space grid: Refinement of the Joslin-Pletcher algorithm. *Journal of Electroanalytical Chemistry and Interfacial Electrochemistry*, 127(1):1–10, 1981.

[31] David Gavaghan. An exponentially expanding mesh ideally suited to the fast and efficient simulation of diffusion processes at microdisc electrodes. 1. Derivation of the mesh. *Journal of Electroanalytical Chemistry*, 456(1):1–12, 1998.

[32] John A Alden and Richard G Compton. A general method for electrochemical simulations. 1. Formulation of the strategy for two-dimensional simulations. *The Journal of Physical Chemistry B*, 101(44):8941–8954, 1997.

[33] Jürgen Heinze. Diffusion processes at finite (micro) disk electrodes solved by digital simulation. *Journal of Electroanalytical Chemistry and Interfacial Electrochemistry*, 124(1-2): 73–86, 1981.

[34] Donald W Peaceman and Henry H Rachford Jr. The numerical solution of parabolic and elliptic differential equations. *Journal of the Society for industrial and Applied Mathematics*, 3(1):28–41, 1955.

[35] Llewellyn Thomas. Elliptic problems in linear differential equations over a network: Watson scientific computing laboratory. *Columbia University, NY*, 1949.

[36] Enno Kätelhön and Richard G Compton. Testing and validating electroanalytical simulations. *Analyst*, 140(8):2592–2598, 2015.

[37] Herbert S Harned and Robert M Hudson. The differential diffusion coefficient of potassium ferrocyanide in dilute aqueous solution at 25. *Journal of the American Chemical Society*, 73(11):5083–5084, 1951.

[38] Charles R Christensen and Fred C Anson. Chronopotentiometry in thin layer of solution. *Analytical Chemistry*, 35(2):205–209, 1963.

[39] Thornton Hubbard. *Electrochemistry in thin layers of solution.* PhD thesis, California Institute of Technology, 1967.

[40] John EB Randles. A cathode ray polarograph. part ii.the current-voltage curves. *Transactions of the Faraday Society*, 44:327–338, 1948.

[41] A Ševčik. Oscillographic polarography with periodical triangular voltage. *Collection of Czechoslovak Chemical Communications*, 13:349–377, 1948.

[42] Martin C Henstridge, Edmund JF Dickinson, and Richard G Compton. Mass transport to and within porous electrodes. Linear sweep voltammetry and the effects of pore size: The prediction of double peaks for a single electrode process. *Russian Journal of Electrochemistry*, 48(6):629–635, 2012.